# A Dual Reference Frame Multistep Direct Model Predictive Current Control With a Disturbance Observer for SPMSM Drives

Xinyue Li, *Graduate Student Member, IEEE*, Qifan Yang, *Graduate Student Member, IEEE*, Wei Tian, *Graduate Student Member, IEEE*, Petros Karamanakos, *Senior Member, IEEE*, and Ralph Kennel, *Senior Member, IEEE*

***Abstract*—The parameter mismatch problem has a great impact on the control performance of model predictive control, which is however unavoidable during the operation. In order to improve the system robustness against the parameter mismatches and disturbances, an improved direct model predictive current control with a disturbance observer is proposed in this article, where the disturbance observer is realized by an incremental moving horizon estimator. Moreover, another concern raised from the applications of direct model predictive current control is the computational burden, especially for the long-horizon implementations. Therefore, a dual reference frame solution for the surface permanent-magnet synchronous motor (SPMSM) is proposed in this article to allocate a great proportion of heavy computations required for the optimization problem to the offline preparation, which can reduce the computational burden by almost 50% on average for a prediction horizon of five time-steps. Besides, the parameter mismatch effects of individual electrical parameters on the control performance of the model predictive direct current control method are investigated and quantified via simulations. A five-step direct model predictive current control is implemented on a dSPACE system with a sampling frequency of 20 kHz to validate the effectiveness of the proposed scheme with an SPMSM drive system.**

***Index Terms*—Disturbance observer, finite-control-set model predictive control (FCS-MPC), permanent-magnet synchronous machine (PMSM), predictive control.**

## I. Introduction

THE permanent-magnet synchronous machine (PMSM) has been widely used in high-performance applications because of its considerable advantages, such as high power density, high efficiency, and good dynamic performance. However, due to the nonlinear nature of the PMSM drive system, adoption of a linear controller, e.g., proportional–integral (PI) control, can hardly obtain satisfactory control performance. To tackle this problem, control methods, such as robust control, fuzzy control, and model predictive control (MPC), have been implemented in the PMSM system. Among them, MPC has received significant attention for the control of power electronics and electrical drives [1], thanks to the advances in microprocessors and efficient numerical optimization methods. It has been applied to various applications [2], [3] because of its advantages, such as the ability to include constraints, the fast dynamic response, and capability to handle the system nonlinearities.

MPC can be roughly divided into two groups: the continuous-control-set model predictive control (CCS-MPC) and the finite-control-set model predictive control (FCS-MPC). CCS-MPC computes the predefined optimization problem for the control problem and requires a modulator to actuate the voltage command. Different from the CCS-MPC, FCS-MPC takes advantage of the discrete nature of the power converters and computes directly the switching states for the inverter. Several comparative studies have been carried out between CCS-MPC and FCS-MPC for ac machine drive systems [4]–[6]. As it is indicated in [5], CCS-MPC has lower requirement on the sampling time and FCS-MPC can achieve faster dynamic performance. Nonetheless, because of the advantages of FCS-MPC, e.g., straightforward implementation, comparatively simple principle, and fast dynamic response, it has been applied for various power converters [7]–[11].

A main disadvantage of FCS-MPC is the computational burden of solving the underlying optimization problem with a long prediction horizon, since the problem is NP-hard, i.e., the computational complexity increases exponentially with the prediction horizon and the voltage levels of the power converter [12]. In many applications, the prediction horizon is chosen to be one, aiming to enable the real-time implementation of FCS-MPC. However, as it is indicated in [13] and [14], MPC benefits from a long prediction horizon in terms of steady-state operation and current distortions. More specifically, a long prediction horizon improves the control performance of FCS-MPC in high-order system more significantly than the one-step alternative. Therefore, several works focusing on reducing the

Manuscript received May 24, 2021; revised August 31, 2021; accepted October 4, 2021. Date of publication October 7, 2021; date of current version November 30, 2021. This work was supported in part by the Deutsche Forschungsgemeinschaft DFG, German Research Foundation under Grant 418870390. Recommended for publication by Associate Editor Navid (GAE) Reza Zargari. *(Corresponding author: Xinyue Li.)*

Xinyue Li is with the Bosch Rexroth AG, 97816 Lohr am Main, Germany (e-mail: xinyue.li@boschrexroth.de).

Qifan Yang, Wei Tian, and Ralph Kennel are with the Institute for Electrical Drive Systems and Power Electronics, Technical University of Munich, 80333 Munich, Germany (e-mail: qifan.yang@tum.de; wei.tian@tum.de; ralph.kennel@tum.de).

Petros Karamanakos is with the Faculty of Information Technology and Communication Sciences, Tampere University, 33101 Tampere, Finland (e-mail: p.karamanakos@ieee.org).

Color versions of one or more figures in this article are available at https://doi.org/10.1109/TPEL.2021.3118572.

Digital Object Identifier 10.1109/TPEL.2021.3118572

computational burden of the long horizon FCS-MPC have been carried out [15]–[17].

Besides, the parameters in PMSMs vary during the operation. For example, the resistance is influenced by the temperature, the inductance can be described as a function of the current, and the permanent magnet flux linkage can be affected by the environmental condition, e.g., the temperature and humidity. Moreover, the manufacturing error exists and is normally restrained within certain tolerance. Therefore, it causes small unbalances among phases. A mathematical analysis has been carried out to analyze the prediction error caused by the parameter uncertainties in a three-phase two-level inverter [18], which indicates that the changes of the load resistance may affect the steady-state error, and the load inductance will have impact on the current ripple as well as on the harmonic distortion. Ortombina *et al.* [19] analyzed the impacts of parameter mismatches on the long-horizon FCS-MPC for a PMSM drive system.

In general, the influence of the parameter mismatch can be attenuated by modifying the controller or by compensating for the related disturbances. In [20], a model-free MPC was proposed to deal with the parameter variation problem. However, in order to tackle the stagnation problem, a minimum refresh frequency is deployed, which can result in a nonoptimum solution of the MPC. An improvement of this method has been given in [21], where the PMSM model is reconstructed based on two most recent current variations. In [22], the parameter mismatch problem was tackled by integrating the prediction errors into the prediction stage. Besides, the robust MPC is also widely applied to improve the system stability. For example, in [23], a Lyapunov-based robust MPC was proposed and validated with experiments. But the robust MPC methods tend to be conservative, which may result in a compromised nominal performance. In [24], a PI cost function was proposed to mitigate the parameter mismatch for FCS-MPC-controlled PMSM drive systems. An alternative for dealing with the parameter mismatch problem is deploying the disturbance observer to estimate the resulted disturbances. Zhang *et al.* [25] employed an incremental prediction model and an inductance disturbance observer, which applied the incremental model to eliminate the influence from the permanent magnet flux linkage and bypassed the impacts from the resistance. A similar methodology was applied to the dual three-phase PMSM system in [26]. An extended high-gain state observer [27] was deployed to estimate the disturbances. Besides, a comprehensive comparison among different disturbance observers was given in [28]. The simulation and experimental results showed that the deployment of the disturbance observer can improve the reference tracking performance and the disturbance rejection ability.

Given the above methods, this article presents an optimal disturbance observer that enhances the robustness of FCS-MPC to model uncertainties over the whole range of operating points. Moreover, to facilitate the real-time implementation of the proposed scheme, a dual reference frame modeling is adopted that manages to not significantly tax the already pronounced computational requirements of long-horizon FCS-MPC. Specifically, the main contributions of this article can be summarized as follows.

1) First, the effects of parameter mismatches on a surface permanent-magnet synchronous motor (SPMSM) drive system under the finite-control-set model predictive current control (FCS-MPCC) are comprehensively simulated. The corresponding quantitative assessment is also given.
2) In order to improve the robustness of the drive system and guarantee the control performance under the existence of any type of disturbances, a moving horizon estimator (MHE) is implemented as disturbance observer, through which the external disturbance is estimated. Consequently, the estimated disturbance is integrated in the direct control problem. MHE formulates the estimation problem as an optimization problem and provides the capability of including the system constraints, thus ensuring effective disturbance rejection.
3) Furthermore, in order to reduce the computational burden of the optimization problem of long-horizon FCS-MPCC and guarantee its real-time feasibility, the control problem of the SPMSM is formulated in the $\alpha\beta$ reference frame. This enables the reduction of the computational burden by allowing for the time-invariant parts of the model to be computed offline, thus greatly alleviating the real-time computational effort.

The rest of this article is organized as follows. The system model of a SPMSM in the $dq$ as well as in the $\alpha\beta$ reference frame is given in Section II. The basics of the long horizon model predictive direct current control, i.e., the cost function and the constraints, are also explained. In Section III, the MHE and the proposed dual reference frame real-time model predictive direct current control with long horizons are presented. The impact of the parameter mismatches on the steady-state error of the tracking problem is shown in Section IV. Subsequently, in Section V, the experimental results investigating the feasibility of the proposed method in real time and its effectiveness against the parameter mismatches are demonstrated and discussed. Finally, Section VI concludes this article.

## II. Problem Formulation

### A. System Model

The mathematical model of a PMSM is formulated in the rotating reference frame in most applications. However, in this article, both reference frames, namely the $dq$ reference frame and the $\alpha\beta$ reference frame, are employed. The $dq$ reference frame is the rotating reference frame, which rotates with the synchronous angular frequency, while the $\alpha\beta$ reference frame is the stationary reference frame. The stator voltage equation of a PMSM in the $dq$ reference frame is first presented, which can be given as

$$\begin{aligned} u_{sd} &= R_{\mathrm{s}}\, i_{sd} + \frac{\mathrm{d}\psi_{sd}}{\mathrm{d}t} - \omega_e \psi_{sq} \\ u_{sq} &= R_{\mathrm{s}}\, i_{sq} + \frac{\mathrm{d}\psi_{sq}}{\mathrm{d}t} + \omega_e \psi_{sd} \end{aligned} \tag{1}$$

where

$$\psi_{\mathrm{s}d} = L_d\, i_d + \Psi_{\mathrm{m}}$$
$$\psi_{\mathrm{s}q} = L_q\, i_q \tag{2}$$

and $\boldsymbol{u}_{\mathrm{s}}$ and $\boldsymbol{i}_{\mathrm{s}}$ denote the voltages and the currents of a PMSM in the $dq$ reference frame, respectively. $R_{\mathrm{s}}$ represents the stator resistance. $\psi_{\mathrm{s}d}$ and $\psi_{\mathrm{s}q}$ are the stator flux linkage in the $d$ and $q$ axes, respectively. $L_d$ and $L_q$ denote the inductance of $d$ and $q$ axes. $\Psi_{\mathrm{m}}$ represents the permanent magnet flux linkage. $\omega_e$ denotes the electrical angular speed.

The PMSM system model in the stationary two-axis reference frame, which is also called the $\alpha\beta$ reference frame, is furthermore given. The system model in the $\alpha\beta$-domain can be derived from (1) via the inverse Park transformation [29]. Since the SPMSM is discussed in this article, where $L_d = L_q$ can be assumed, the equations in (1) can be written in the $\alpha\beta$ reference frame as

$$\begin{bmatrix} u_{\mathrm{s}\alpha} \\ u_{\mathrm{s}\beta} \end{bmatrix} = \begin{bmatrix} R_{\mathrm{s}} & 0 \\ 0 & R_{\mathrm{s}} \end{bmatrix} \begin{bmatrix} i_{\mathrm{s}\alpha} \\ i_{\mathrm{s}\beta} \end{bmatrix} + \begin{bmatrix} L_s & 0 \\ 0 & L_s \end{bmatrix} \begin{bmatrix} \frac{\mathrm{d}i_\alpha}{\mathrm{d}t} \\ \frac{\mathrm{d}i_\beta}{\mathrm{d}t} \end{bmatrix} + \omega_e \Psi_{\mathrm{m}} \begin{bmatrix} -\sin(\theta_e) \\ \cos(\theta_e) \end{bmatrix}. \tag{3}$$

The system model of an SPMSM in the $dq$ reference frame given in (1) can be discretized via the forward Euler method and rewritten in a compact form as

$$\boldsymbol{x}_{k+1}^F = \boldsymbol{A}^F \boldsymbol{x}_k^F + \boldsymbol{B}^F \boldsymbol{u}_k^F + \boldsymbol{E}_k^F$$
$$\boldsymbol{y}_k^F = \boldsymbol{C} \boldsymbol{x}_k^F \tag{4}$$

where superscript $F$ denotes the $dq$ reference frame. $\boldsymbol{x}$ and $\boldsymbol{y}$ represent the system states and measurements, respectively. They are given as $[i_d\, i_q]^T$. $\boldsymbol{u}_k^F$ denotes the voltage $[u_d\, u_q]^T$, which is transformed from three-phase switch states $\boldsymbol{v}$ via the Park transformation. $\boldsymbol{E}^F$ is the term including the permanent magnet flux linkage $\Psi_{\mathrm{m}}$, which is denoted by $[0\ -\omega_e T_{\mathrm{s}} \frac{\Psi_{\mathrm{m}}}{L_q}]^T$. $T_{\mathrm{s}}$ denotes the sampling interval.

Analogously, the system model of an SPMSM in the $\alpha\beta$ domain can be rewritten as

$$\boldsymbol{x}_{k+1}^S = \boldsymbol{A}^S \boldsymbol{x}_k^S + \boldsymbol{B}^S \boldsymbol{T}_c\, \boldsymbol{v}_k + \boldsymbol{E}_k^S$$
$$\boldsymbol{y}_k^S = \boldsymbol{C} \boldsymbol{x}_k^S \tag{5}$$

where superscript $S$ denotes the $\alpha\beta$ reference frame. $\boldsymbol{T}_c$ denotes the Clarke transformation, which transforms the quantity in three-phase domain into $\alpha\beta$ domain. The states and the measured output are given as $\boldsymbol{x}^S := [i_\alpha\, i_\beta]^T$ and $\boldsymbol{y}^S := [i_\alpha\, i_\beta]^T$, respectively. $\boldsymbol{v}$ denotes the switching states of three phases, i.e., $\boldsymbol{v} := [v_a\, v_b\, v_c]^T$.

### *B. Long Horizon Direct Model Predictive Current Control*

The direct model predictive controller, which is also referred as FCS-MPC, aims to compute the switching signals for the inverter. As it is indicated in [13], a long prediction horizon of MPC is beneficial for closed-loop stability and the control performance. However, the most applied method to solve the reference tracking problem arisen from the direct current control problem of PMSM is the exhaustive enumeration. Its computational complexity increases exponentially with the dimension of the optimizer [12]. In [15], an efficient approach is proposed to reduce the computational burden of FCS-MPC with the long prediction horizon. In this article, the symmetry of the SPMSM in the $\alpha\beta$ reference frame is utilized to further reduce the computational burden, which can be regarded as a further improvement regarding the computational efficiency based on the work in [30].

The long-horizon model predictive direct current control for an SPMSM drive system can be formulated as an optimization problem $\mathcal{P}_c$ in the following [15]:

$$\begin{aligned} \underset{\boldsymbol{V}}{\text{minimize}} J = & \sum_{j=k}^{k+N_p-1} \|\boldsymbol{y}_{r,\,j+1} - \boldsymbol{C}\, \boldsymbol{x}_{j+1}^S \\ & \|_2^2 + \lambda \|\boldsymbol{v}_j - \boldsymbol{v}_{j-1}\|_2^2 \\ \text{subject to} \boldsymbol{x}_{j+1}^S = & \boldsymbol{A}^S\, \boldsymbol{x}_j^S + \boldsymbol{B}^S\, \boldsymbol{T}_c\, \boldsymbol{v}_j + \boldsymbol{E}^S \\ & \boldsymbol{v}_j \in \mathbb{V} \times \mathbb{V} \times \mathbb{V} \end{aligned} \tag{6}$$

where $N_p$ is the prediction horizon. $\boldsymbol{V}_k$ denotes the control sequence and can be given as $\boldsymbol{V}_k := [\boldsymbol{v}_k^T\, \boldsymbol{v}_{k+1}^T\, \ldots\, \boldsymbol{v}_{k+N_p-1}^T]^T$. $\mathbb{V}$ is the feasible set of the control output, which can be given as

$$\mathbb{V} := \{-1,\, 1\} \tag{7}$$

for the two-level inverter.

## III. Proposed Dual Reference Frame Real-Time FCS-MPCC

The underlying optimization problem includes the system model as the constraint, as presented in (6). This characteristic of the FCS-MPCC results in the sensitivity of the FCS-MPCC to the model inaccuracy. An MHE-based disturbance observer is employed in this article to improve the system robustness against the parameter mismatches. MHE exhibits high dynamic performance and is capable to handle the system constraints. Many works have shown the superiority of MHE over other estimators [31], [32]. The overall block diagram of the proposed dual reference frame real-time long-horizon robust finite-control-set model predictive current control (RFCS-MPCC) is shown in Fig. 1.

The disturbance observer delivers the estimated current and the disturbance to the controller, where the estimator is established in the $dq$ domain to guarantee the estimation accuracy, and the controller is set up in the $\alpha\beta$ domain to reduce the computational burden in real time.

### *A. Moving Horizon Estimator*

The MHE is implemented to estimate the disturbance caused by the parameter mismatch, of which the estimation accuracy is guaranteed by formulating the estimator in the $dq$ reference frame. This is because the estimation of a constant value is in general easier than the estimation of a varying value. The incremental MHE for the estimation can be formulated as an

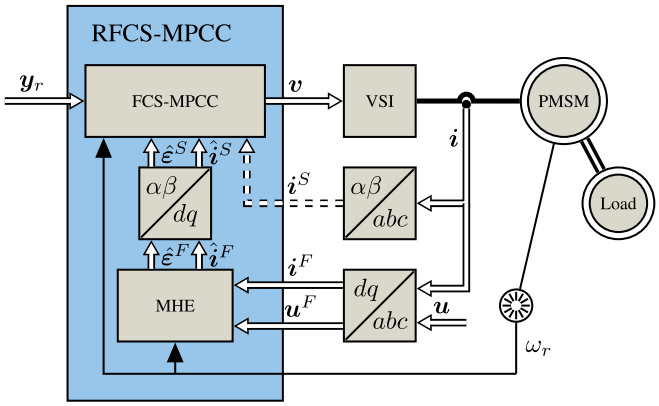


Fig. 1. Proposed RFCS-MPCC strategy for the reference tracking in PMSM drive system.

optimization problem $\mathcal{P}_e$ at time $k$ over a horizon of $N_e$ and is written as [33]

$$\begin{aligned} \underset{\hat{\boldsymbol{x}},\,\Delta\hat{\boldsymbol{\varepsilon}}}{\text{minimize}} \quad & J_{obs} \\ \text{subject to} \quad & \hat{\boldsymbol{x}}^F_{j+1} = \boldsymbol{A}^F \hat{\boldsymbol{x}}^F_j + \boldsymbol{B}^F \boldsymbol{u}^F_j + \boldsymbol{E}^F + \hat{\boldsymbol{\varepsilon}}^F_j \\ & \hat{\boldsymbol{\varepsilon}}^F_{j+1} = \hat{\boldsymbol{\varepsilon}}^F_k + \Delta\hat{\boldsymbol{\varepsilon}}^F_j \end{aligned} \tag{8}$$

where

$$J_{obs} = \sum_{j=k-N_e+1}^{k} \|\boldsymbol{y}^F_j - \boldsymbol{C}\hat{\boldsymbol{x}}^F_j\|^2_{\boldsymbol{Q}} + \sum_{j=k-N_e+1}^{k-1} \|\Delta\hat{\boldsymbol{\varepsilon}}^F_j\|^2_{\boldsymbol{R}}.$$

The optimization problem $\mathcal{P}_e$ in (8) is then sorted as a matrix formulation after substituting the system state-space model into the cost function, which can be given as

$$J_{obs} = (\boldsymbol{Y}^F - \hat{\boldsymbol{Y}}^F)^T \boldsymbol{Q}\,(\boldsymbol{Y}^F - \hat{\boldsymbol{Y}}^F) + (\Delta\hat{\boldsymbol{\mathcal{E}}}^F)^T \boldsymbol{R}\,\Delta\hat{\boldsymbol{\mathcal{E}}}^F \tag{9}$$

where $\boldsymbol{Y}^F$ is the sequence of measurements, which can be written as $\boldsymbol{Y}^F := [\boldsymbol{y}^T_{k-N_e+1}\,\boldsymbol{y}^T_{k-N_e+2}\,\cdots\,\boldsymbol{y}^T_k]^T$, $\Delta\hat{\boldsymbol{\mathcal{E}}}$ is the sequence of the disturbance increments over the estimating horizon, which can be denoted by $\Delta\hat{\boldsymbol{\mathcal{E}}} := [\Delta\hat{\boldsymbol{\varepsilon}}^T_{k-N_e+1}\,\Delta\hat{\boldsymbol{\varepsilon}}^T_{k-N_e+2}\,\cdots\,\Delta\hat{\boldsymbol{\varepsilon}}^T_k]^T$. $\hat{\boldsymbol{Y}}$ is the sequence of the estimations on the output variables, which is defined as $\hat{\boldsymbol{Y}} := [\hat{\boldsymbol{y}}^T_{k-N_e+1}\,\hat{\boldsymbol{y}}^T_{k-N_e+2}\,\cdots\,\hat{\boldsymbol{y}}^T_k]^T$. Furthermore, $\hat{\boldsymbol{Y}}$ can be formulated as a function of the initial value of the estimated state $\hat{\boldsymbol{x}}_k$, the sequence of the applied voltage $\boldsymbol{U} := [\boldsymbol{u}^F_{k-N_e+1}{}^T\,\boldsymbol{u}^F_{k-N_e+2}{}^T\,\cdots\,\boldsymbol{u}^F_k{}^T]^T$, and the estimated disturbance $\hat{\boldsymbol{\varepsilon}}_k$ as

$$\hat{\boldsymbol{Y}}^F = \boldsymbol{\Pi}^F\,\hat{\boldsymbol{x}}^F_k + \boldsymbol{\Lambda}^F\,\boldsymbol{U}^F + \boldsymbol{\Sigma}^F\,(\boldsymbol{E}^F + \hat{\boldsymbol{\varepsilon}}^F_k) + \boldsymbol{\Phi}^F \Delta\hat{\boldsymbol{\mathcal{E}}}^F \tag{10}$$

where $\boldsymbol{\Pi}^F$, $\boldsymbol{\Lambda}^F$, $\boldsymbol{\Sigma}^F$, and $\boldsymbol{\Phi}^F$ are given in the Appendix. The problem $\mathcal{P}_e$ is then solved with

$$\nabla_{\Delta\hat{\boldsymbol{\mathcal{E}}}^F} J_{obs} = \boldsymbol{0}. \tag{11}$$

By substituting (10) into (9), the solution of (11) can be derived as

$$\Delta\hat{\boldsymbol{\mathcal{E}}}^F = ((\boldsymbol{\Phi}^F)^T\,\boldsymbol{Q}\,\boldsymbol{\Phi}^F + \boldsymbol{R})^{-1}(\boldsymbol{\Phi}^F)^T\boldsymbol{Q}\,\boldsymbol{\xi} \tag{12}$$

where

$$\boldsymbol{\xi} = \boldsymbol{Y}^F - \boldsymbol{\Pi}^F\,\hat{\boldsymbol{x}}^F_k - \boldsymbol{\Lambda}^F\,\boldsymbol{U}^F - \boldsymbol{\Sigma}^F\,(\boldsymbol{E}^F + \hat{\boldsymbol{\varepsilon}}^F_k). \tag{13}$$

Here it is important to point out that the stability of MHE has been addressed in works such as [34]. Hence, by properly designing the MHE scheme, the asymptotic stability is ensured [34].

### *B. Real-Time Long Horizon Model Predictive Direct Current Control*

After obtaining the estimates $\hat{\boldsymbol{x}}^F$ and $\hat{\boldsymbol{\varepsilon}}^F$ from the aforementioned MHE, the inverse Park transformation is deployed to transform the quantity from the $dq$ reference frame to the $\alpha\beta$ reference frame. The Park transformation is given by $\boldsymbol{x}_{dq} = \boldsymbol{T}_p\,\boldsymbol{x}_{\alpha\beta}$ with

$$\boldsymbol{T}_p = \begin{bmatrix} \cos\theta_e & \sin\theta_e \\ -\sin\theta_e & \cos\theta_e \end{bmatrix}. \tag{14}$$

The optimization problem in (6) is then reformulated for the RFCS-MPCC by replacing the currents and the disturbance with their estimates and extrapolating them within the prediction horizon. RFCS-MPCC is then given as

$$\begin{aligned} \underset{\boldsymbol{V}}{\text{minimize}} J = & \sum_{j=k}^{k+N_p-1} \|\boldsymbol{y}_{r,\,j+1} - \boldsymbol{C}\,\hat{\boldsymbol{x}}_{j+1} \\ & \|^2_2 + \lambda\|\boldsymbol{v}_j - \boldsymbol{v}_{j-1}\|^2_2 \\ & \text{subject to} \hat{\boldsymbol{x}}^S_{j+1} = \boldsymbol{A}^S\,\hat{\boldsymbol{x}}^S_j + \boldsymbol{B}^S\,\boldsymbol{T}_c\,\boldsymbol{v}_j + \boldsymbol{E}^S + \hat{\boldsymbol{\varepsilon}}^S_j \\ & \boldsymbol{v}_j \in \mathbb{V} \times \mathbb{V} \times \mathbb{V}. \end{aligned} \tag{15}$$

The cost function in (15) is then reformulated regarding the control sequence $\boldsymbol{V}_k$ as

$$J = \theta_k + 2(\boldsymbol{\Theta}_k)^T\boldsymbol{V}_k + \|\boldsymbol{V}_k\|^2_{\boldsymbol{H}_t} \tag{16}$$

where

$$\begin{aligned} \theta_k &:= \|\boldsymbol{Y}_r - \boldsymbol{\Pi}^S\,\hat{\boldsymbol{x}}_k - \boldsymbol{\Phi}^S\,\boldsymbol{T}\,(\boldsymbol{E}^F + \hat{\boldsymbol{\varepsilon}}^F_k)\|^2_2 + \lambda\|\boldsymbol{\delta}\boldsymbol{v}_{k-1}\|^2_2 \\ \boldsymbol{\Theta}_k &:= ((\boldsymbol{Y}_r - \boldsymbol{\Pi}^S\hat{\boldsymbol{x}}_k - \boldsymbol{\Phi}^S\boldsymbol{T}(\boldsymbol{E}^F + \hat{\boldsymbol{\varepsilon}}^F_k))^T\boldsymbol{\Upsilon} \\ &\quad - \lambda(\boldsymbol{\delta}\boldsymbol{v}_{k-1})^T\boldsymbol{S})^T \\ \boldsymbol{H}_t &:= \boldsymbol{\Upsilon}^T\boldsymbol{\Upsilon} + \lambda\,\boldsymbol{S}^T\boldsymbol{S} \end{aligned}$$

where $\boldsymbol{Y}_r$ denotes the output reference trajectory over the prediction horizon $N_p$. The matrices $\boldsymbol{\Pi}^S$, $\boldsymbol{\Phi}^S$, $\boldsymbol{\Upsilon}$, $\boldsymbol{S}$, $\boldsymbol{T}$, and $\boldsymbol{\delta}$ are given in the Appendix.

Analogously to the article presented in [15], the optimization problem in (15) can be simplified and rewritten more compactly as a problem finding

$$\boldsymbol{V}^* = \arg\min_{\boldsymbol{V}_k} \|\boldsymbol{H}\boldsymbol{V}_k - \bar{\boldsymbol{V}}_k\|^2_2 \tag{17}$$

where $\boldsymbol{H}^T\boldsymbol{H} = \boldsymbol{H}_t$ and $\bar{\boldsymbol{V}}_k := \boldsymbol{H}(-\boldsymbol{H}_t^{-1}\,\boldsymbol{\Theta}_k)$. It is worth mentioning that the matrices $\boldsymbol{\Pi}^S$, $\boldsymbol{\Phi}^S$, and $\boldsymbol{\Upsilon}$ can be computed offline, since they are only related to the system matrix $\boldsymbol{A}^S$, the input matrix $\boldsymbol{B}^S$, the output matrix $\boldsymbol{C}$, and the Clarke transformation matrix $\boldsymbol{T}_c$, which are time-invariant. Therefore,

**Procedure 1:** Computation Procedure of RFCS-MPCC.

1: Compute the matrices $\mathbf{\Pi}^S$, $\mathbf{\Phi}^S$, and $\mathbf{\Upsilon}$, and, consequently, $\boldsymbol{H}_t^{-1}$ and $\boldsymbol{H}$
2: **while** online **do**
3: Measure the current
4: **if** MHE is activated **then**
5: Solve the optimization problem in (8) to obtain $\hat{\boldsymbol{\varepsilon}}^F$ and $\hat{\boldsymbol{i}}^F$
6: Transform the $dq$ quantities into the $\alpha\beta$-frame, i.e., acquire $\hat{\boldsymbol{\varepsilon}}^S$ and $\hat{\boldsymbol{i}}^S$, and feed them into the current controller
7: **end if**
8: Solve the optimization problem (15)
9: Deliver $\boldsymbol{v}^*$ to the inverter
10: **end while**

the computation of the intermediate matrices $\boldsymbol{H}_t^{-1}$ and $\boldsymbol{H}$ is then allocated offline, which reduces the online computational burden significantly. After constructing the optimization problem, the problem in (15) is then solved with the sphere-decoding algorithm in [15]. The complete procedure, that describes the tasks performed offline and in real time, is given in Procedure 1.

## IV. Impact of the Parameter Mismatches

The effect of the parameter mismatches on the SPMSM is studied via theoretical analysis and simulations in this section. The parameters of the real PMSM drive system may differ from the those used in the controller. On the one hand, the environmental conditions, e.g., the temperature and the humidity, have influence on the parameter value. On the other hand, the working conditions can also affect the machine parameters. The conventional FCS-MPCC is established on the nominal system model, where the nominal parameters that are either measured offline or directly obtained from the manufacturer's data sheet are employed. Therefore, the control performance can deteriorate due to the parameter mismatches [19]. Recall the nominal current prediction model based on (3), the current predictions including the parameter mismatch effect can be given as

$$\begin{aligned} i_{\alpha,\,k+1} = &\left(1-\frac{R_\mathrm{s}+\Delta R}{L_0+\Delta L}T_s\right) i_{\alpha,\,k} \\ &+\frac{\omega_e\left(\Psi_\mathrm{m}+\Delta\Psi\right)}{L_0+\Delta L}T_s\,\sin(\theta_e)+\frac{T_s}{L_0+\Delta L}u_{\alpha,\,k} \\ i_{\beta,\,k+1} = &\left(1-\frac{R_\mathrm{s}+\Delta R}{L_0+\Delta L}T_s\right) i_{\beta,\,k} \\ &-\frac{\omega_e\left(\Psi_\mathrm{m}+\Delta\Psi\right)}{L_0+\Delta L}T_s\,\cos(\theta_e)+\frac{T_s}{L_0+\Delta L}u_{\beta,\,k} \end{aligned} \tag{18}$$

where $\Delta R$, $\Delta L$, and $\Delta\Psi$ denote the bias of the parameters. The prediction error accumulates as the prediction horizon increases. However, because of the inclusion of the discrete nature of the inverter and the implementation of the receding horizon policy in FCS-MPCC, the impact of the parameter mismatch is difficult to be quantified through theoretical analysis. Therefore, simulations are conducted, which aims to quantify the resulted control performance of the FCS-MPCC.

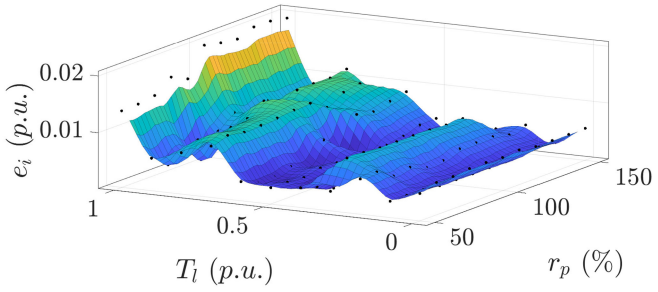


Fig. 2. Steady-state error $e_i$ caused by the parameter mismatch of $R_\mathrm{s}$ for the FCS-MPCC with $N_p = 1$.

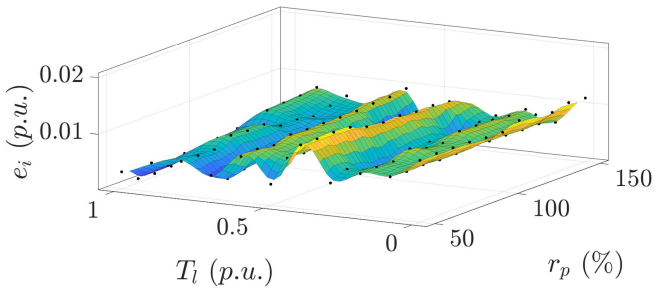


Fig. 3. Steady-state error $e_i$ caused by the parameter mismatch of $R_\mathrm{s}$ for the FCS-MPCC with $N_p = 5$.

The corresponding simulation results are shown in the following, where the simulations are designed based on different rates of parameter change and various working points. The ratio $r_p$ is applied to indicate the relationship between the parameter values in the controller and their actual value, which is given by

$$r_p = \frac{p_c}{p_m}\times 100\% \tag{19}$$

where $p_c$ is the value of the parameter in the current controller and $p_m$ is that in the motor. The effect of the parameter mismatch is quantified by the steady-state offset $e_i$, which is computed by

$$e_i = \frac{\|\boldsymbol{i}-\boldsymbol{i}_r\|_2}{I_N} \tag{20}$$

where $\boldsymbol{i}$ denotes the measured current, $\boldsymbol{i}_r$ is the reference current, and $I_N$ is the rated current. Different scenarios are tested for both $N_p = 1$ and $N_p = 5$. The simulation results are summarized and illustrated in Figs. 2–7, where the actual values $\boldsymbol{e}_i$ are denoted by black dots and the maps are fitted in MATLAB. The simulations are carried out at a switching frequency around 1.5 kHz.

The impact from the $R_\mathrm{s}$ mismatch is presented in Fig. 2 for $N_p = 1$ and in Fig. 3 for $N_p = 5$. It can be noted that in the context of the $R_\mathrm{s}$ mismatch, the rate of the parameter mismatch $r_p$ has less impact than the load condition on the steady-state error. Moreover, the relationship between the load condition and the steady-state error at the same rate of $R_\mathrm{s}$ change is nonlinear. For the one-step control, the largest error appears at full-load condition, while it can be found at no-load condition for $N_p = 5$.

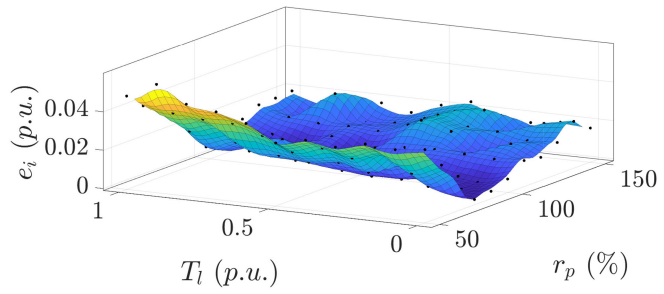


Fig. 4. Steady-state error $e_i$ caused by the parameter mismatch of $L_\mathrm{s}$ for the FCS-MPCC with $N_p = 1$.

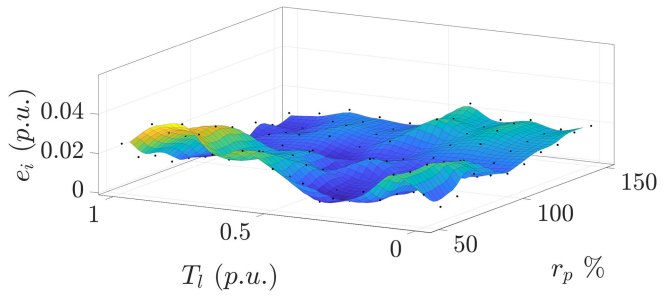


Fig. 5. Steady-state error $e_i$ caused by the parameter mismatch of $L_\mathrm{s}$ for the FCS-MPCC with $N_p = 5$.

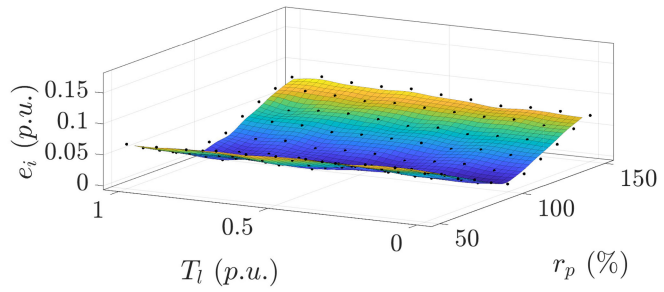


Fig. 6. Steady-state error $e_i$ caused by the parameter mismatch of $\Psi_\mathrm{m}$ for the FCS-MPCC with $N_p = 1$.

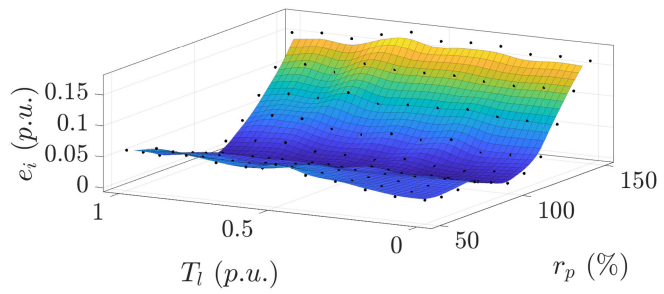


Fig. 7. Steady-state error $e_i$ caused by the parameter mismatch of $\Psi_\mathrm{m}$ for the FCS-MPCC with $N_p = 5$.

Furthermore, the impact of the $L_\mathrm{s}$ mismatch is investigated. Different from the CCS-MPC, for which $L_\mathrm{s}$ can affect the closed-loop system stability, FCS-MPC remains stable under the parameter mismatch of $L_\mathrm{s}$ [35]. It can be explained by the fact that the FCS-MPC directly employs the discrete nature of the inverter and therefore less sensitive to the model accuracy than the CCS-MPC. Moreover, the parameter mismatch of $L_\mathrm{s}$ can induce larger steady-state error than $R_\mathrm{s}$, which amounts up to 4% for $N_p = 1$ and more than 3% for $N_p = 5$. It can be observed from Fig. 4 that the rate of parameter mismatch has a positive relationship with the steady-state error, but this relationship is not symmetric about $r_p = 100\%$, which can be traced back to the fact that the term associated with $L_\mathrm{s}$ appears at the denominator in (18). This asymmetry is more obvious in Fig. 5. More specifically, the relationship between the rate of change and the steady-state error is rather nonlinear. Different from $R_\mathrm{s}$, the largest steady-state error caused by $L_\mathrm{s}$ mismatch can be found at the full-load and $r_p = 50\%$ for both one-step and multistep FCS-MPCC. It can be noted from Figs. 6 and 7 that the parameter mismatch of $\Psi_\mathrm{m}$ causes more steady-state error for the FCS-MPCC with $N_p = 5$ than for the FCS-MPCC with $N_p = 1$. For the one-step FCS-MPCC, the variation of $\Psi_\mathrm{m}$ in a range from $r_p = 50\%$ to $r_p = 150\%$ can result in a steady-state error up to 8% of the rated current. Nonetheless, it can cause a steady-state error of FCS-MPCC with $N_p = 5$ up to almost 15% of the rated value. Different from the simulation results of $L_\mathrm{s}$ mismatch, the steady-state error resulted from the $\Psi_\mathrm{m}$ mismatch is symmetric about $r_p = 100\%$ for $N_p = 1$ and positively related to $r_p$ for $N_p = 5$.

Conclusions can be drawn from the simulation results and the associated observations. First, the stator resistance has the least impact on the control performance of FCS-MPCC, while the permanent magnet flux linkage can cause the largest steady-state error. Moreover, the influence from the parameter variation of $R_\mathrm{s}$ and $L_\mathrm{s}$ is nonlinear with respect to the operating condition. On the contrary, the steady-state error resulted from the parameter variation of $\Psi_\mathrm{m}$ is nearly linear with respect to the load torque. For a certain load condition, the steady-state error is positively dependent on the ratio of the $\Psi_\mathrm{m}$ variation.

## V. Experimental Evaluation

The proposed RFCS-MPCC and the conventional FCS-MPCC are implemented on a dSPACE system, in order to validate the feasibility of the formulated optimization problem in real-time application and the effectiveness of the proposed RFCS-MPCC against the parameter mismatches. The dSPACE SCALEXIO real-time system consists of a 4 GHz Intel XEON processor and a Xilinx Kintex-7 field-programmable gate array. The drive system comprises a SEW-MDX inverter and a 1024-ppr incremental encoder. The sampling time is set to $T_s = 50\,\mu$s. The dc-link voltage is around 560 V. The investigated PMSM is coupled with an induction machine (IM) rated 2.2 kW. The parameters of the PMSM are given in Table I.

The proposed RFCS-MPCC and the conventional FCS-MPCC were tested under various scenarios, i.e., the parameter mismatch of $\Psi_\mathrm{m}$ and $L_\mathrm{s}$ with $r_p = 50\%$ as well as with $r_p = 150\%$. However, only the experimental results of $r_p = 50\%$ are included to keep the presentation of the results and the subsequent impact on the control performance succinct, concise, and simple. Similar conclusions for the results of $r_p = 150\%$ can be drawn from $r_p = 50\%$. Therefore, the results of $r_p = 150\%$ are omitted. A load step from 0% to 50% of the rated torque is

TABLE I
PARAMETERS OF PMSM

| Parameter | Symbol | PMSM |
|---|---|---|
| Rated voltage | $U_N$ | 380 V |
| Rated current | $I_N$ | 6.3 A |
| Rated speed | $w_{mN}$ | 3000 rpm |
| Rated torque | $T_N$ | 10.5 N m |
| Number of pole pairs | $n_\mathrm{p}$ | 3 |
| Nominal permanent flux | $\Psi_\mathrm{m}$ | 0.26 Wb |
| Nominal phase resistance | $R_\mathrm{s}$ | 0.95 Ω |
| Nominal inductance | $L_s$ | 9.6 mH |

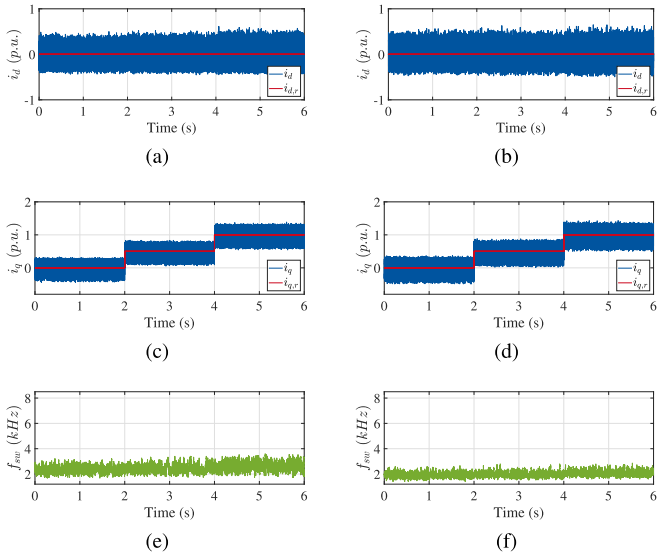


Fig. 8. Comparison between the RFCS-MPCC and FCS-MPCC with $N_p = 1$ under the nominal condition. The figures of the left column denote the performance of FCS-MPCC and the figures of the right column represent the control performance of the proposed RFCS-MPCC. (a) and (b) Tracking performance of $d$-current. (c) and (d) represent the tracking performance of $q$-current. (e) and (f) Switching frequencies.

added at $t = 2\,\mathrm{s}$ and another load step from 50% to full load is conducted at $t = 4\,\mathrm{s}$.

### A. Performance Under the Nominal Condition

First, both methods are tested under the nominal condition, i.e., with the nominal parameters listed in Table I. The experimental results are shown in Figs. 8 and 9. They indicate the comparison under the $N_p = 1$ control and the $N_p = 5$ control, respectively. It can be observed from Fig. 8 that the FCS-MPCC and RFCS-MPCC yield similar performance under the nominal condition with $N_p = 1$ and $N_p = 5$. Moreover, in Fig. 9, a similar phenomenon can be observed. However, a smaller current ripple during steady state with RFCS-MPCC is worth mentioning.

### B. Performance Under the Variation of $\Psi_m$

The first validating scenario is the parameter variation of the permanent magnet flux linkage $\Psi_\mathrm{m}$. The measurements under

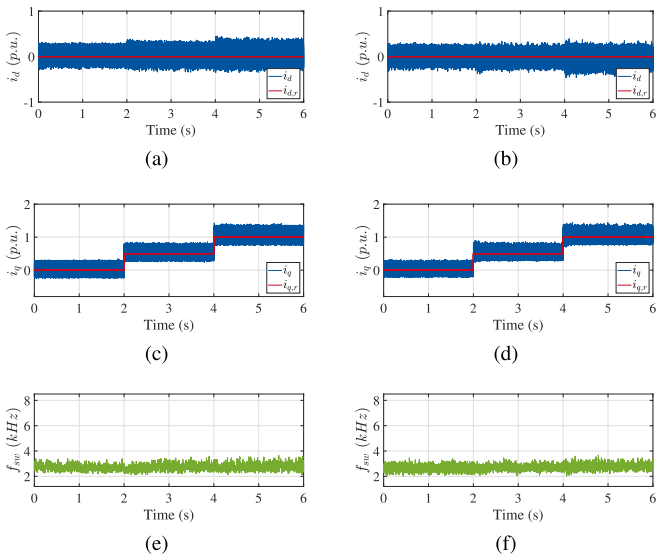


Fig. 9. Comparison between the RFCS-MPCC and FCS-MPCC with $N_p = 5$ under the nominal condition. The figures of the left column denote the performance of FCS-MPCC and the figures of the right column represent the control performance of the proposed RFCS-MPCC.

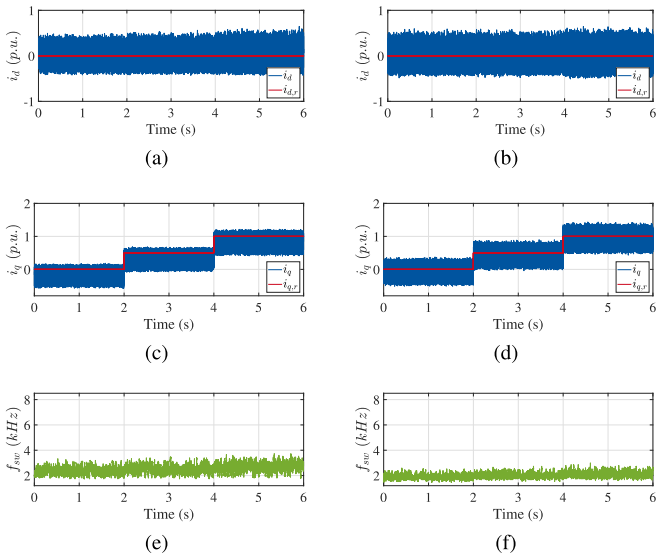


Fig. 10. Comparison between the RFCS-MPCC and FCS-MPCC with $N_p = 1$ under the parameter mismatch of $\Psi_\mathrm{m}$ with $r_p = 50\%$. The figures of the left column denote the performance of FCS-MPCC and the figures of the right column represent the control performance of the proposed RFCS-MPCC.

$r_p = 50\%$ are presented in Fig. 10 for $N_p = 1$ and in Fig. 11 for $N_p = 5$. It can be noted from Figs. 10 and 11 that the decrease of the $\Psi_\mathrm{m}$ value generates a negative steady-state offset. More specifically, a steady-state error around 25% of the rated current in $q$-axis can be observed at $N_p = 1$, which is around 13% of the rated current at $N_p = 5$. On the $d$-axis, a steady-state error can also be noticed, which, however, is smaller than that on the $q$-axis. Nonetheless, the implementation of the proposed RFCS-MPCC mitigates the steady-state error caused by the decrease of $\Psi_\mathrm{m}$ effectively.

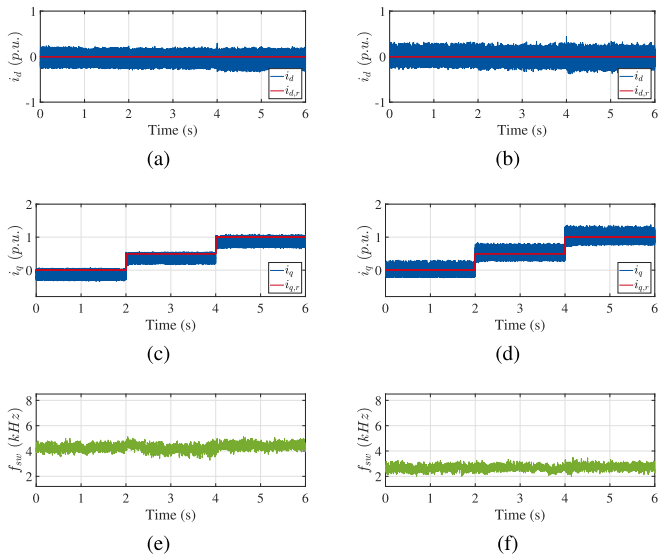


Fig. 11. Comparison between the RFCS-MPCC and FCS-MPCC with $N_p = 5$ under the parameter mismatch of $\Psi_{\mathrm{m}}$ with $r_p = 50\%$. The figures of the left column denote the performance of FCS-MPCC and the figures of the right column represent the control performance of the proposed RFCS-MPCC.

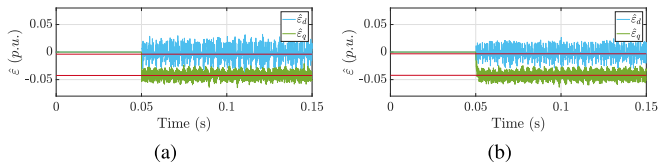


Fig. 12. Estimated disturbance $\hat{\varepsilon}$ with RFCS-MPCC for both (a) $N_p = 1$ and (b) $N_p = 5$. The real value of the disturbance is shown in red, while the estimated disturbance on the $d$-axis is denoted in light blue and the estimated disturbance on the $q$-axis is shown in green.

Moreover, the convergence of the estimated disturbance is shown in Fig. 12 for both cases $N_p = 1$ and $N_p = 5$, while the drive system is being operated at steady state with $i_d = 0$ per unit (p.u.) and $i_q = 1$ p.u. and the initial values of the estimator are zeros. The MHE is activated at $t = 0.05\,\mathrm{s}$. As it is shown in the figure, the estimated disturbance quickly converges to the new steady state after the activation of the estimator.

### C. Performance Under the Variation of $L_s$

FCS-MPCC and RFCS-MPCC are further tested under the parameter mismatch of $L_{\mathrm{s}}$. The experimental results of $r_p = 50\%$ are shown in Figs. 13 and 14, respectively.

Steady-state errors can also be observed under the variation of $L_{\mathrm{s}}$. More conspicuous steady-state errors than at the variation of $\Psi_{\mathrm{m}}$ are shown in Figs. 13 and 14. A steady-state error of around 40% of the rated current is evoked on the $q$-axis for $N_p = 1$, which increases to about 50% of $I_N$ for $N_p = 5$, i.e., the control performance under $N_p = 5$ has larger error than $N_p = 1$. Moreover, the steady-state errors can also be observed on the $d$-axis, when the system is controlled with FCS-MPCC. The corresponding switching frequencies have also been influenced. However, the deployment of the proposed RFCS-MPCC can

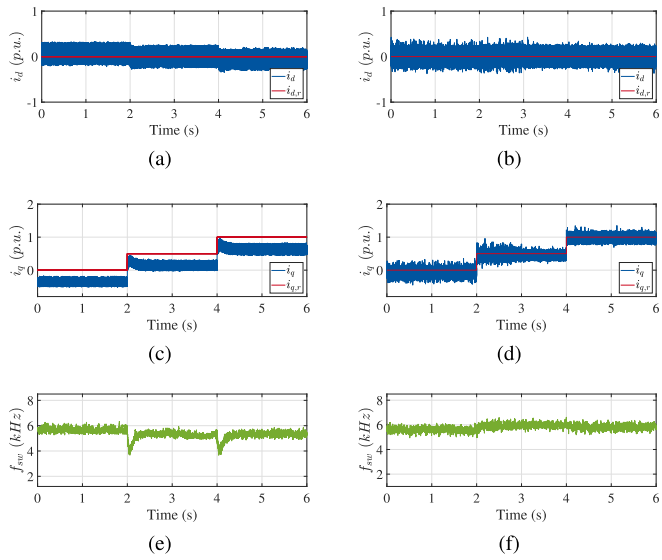


Fig. 13. Comparison between the RFCS-MPCC and FCS-MPCC with $N_p = 1$ under the parameter mismatch of $L_{\mathrm{s}}$ with $r_p = 50\%$. The figures of the left column denote the performance of FCS-MPCC and the figures of the right column represent the control performance of the proposed RFCS-MPCC.

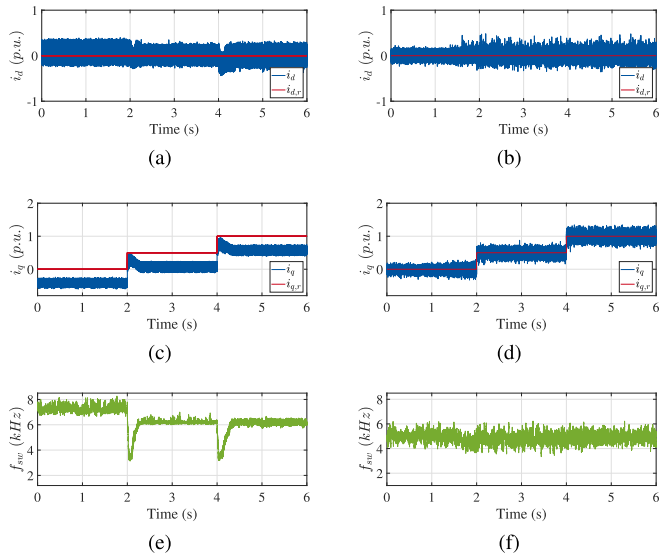


Fig. 14. Comparison between the RFCS-MPCC and FCS-MPCC with $N_p = 5$ under the parameter mismatch of $L_{\mathrm{s}}$ with $r_p = 50\%$. The figures of the left column denote the performance of FCS-MPCC and the figures of the right column represent the control performance of the proposed RFCS-MPCC.

effectively eliminate any steady-state errors and stabilizes the switching frequencies under the existence of the $L_{\mathrm{s}}$ mismatch.

### D. Total Demand Distortion

Furthermore the total demand distortion (TDD) of the FCS-MPCC and of the RFCS-MPCC is investigated, since the current quality is an important metric for evaluating the control performance of the direct current controller. TDD is computed based on the nominal current. Therefore, it is immune to potential tracking errors and fairly demonstrates the harmonic content.

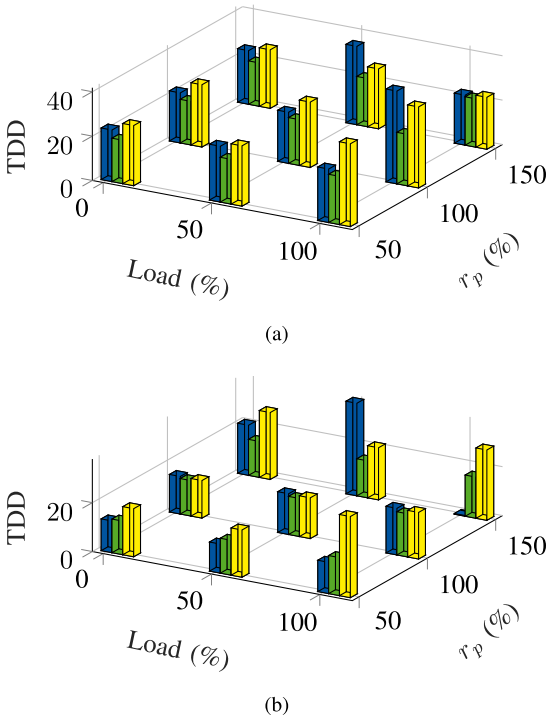


Fig. 15. Comparison of the TDD under the parameter mismatch of $\Psi_{\mathrm{m}}$, where the blue and the green denote the TDD with switching frequencies shown in previous testing scenarios of FCS-MPCC and the proposed RFCS-MPCC, respectively, and the yellow represents the TDD of FCS-MPCC with the mean switching frequency same as that of the RFCS-MPCC in previous scenarios. (a) Control of $N_p = 1$. (b) Results from the control of $N_p = 5$.

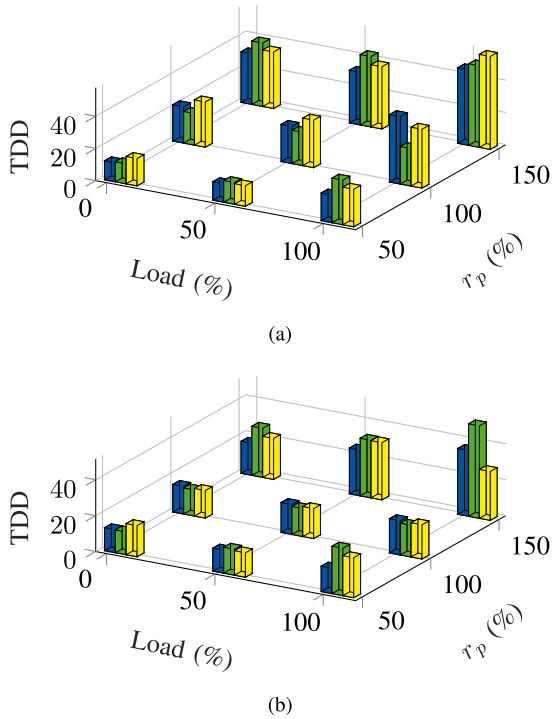


Fig. 16. Comparison of the TDD under the parameter mismatch of $L_{\mathrm{s}}$. (a) and (b) Results from the current control of $N_p = 1$ and $N_p = 5$, respectively.

The TDD is computed with

$$\mathrm{TDD} = \frac{1}{\sqrt{2}\, I_N} \sqrt{\sum_{j \neq 1} i_{s,j}^2} \tag{21}$$

where $j$ denotes the order of the current harmonics. The results are shown in Figs. 15 and 16, where Fig. 15 shows the impact from the parameter variation of $\Psi_{\mathrm{m}}$ and Fig. 16 represents the results under the variation of $L_{\mathrm{s}}$.

It is worth mentioning that at $r_p = 150\%$ and full-load condition, the TDD value of FCS-MPCC is exceptional small, because the PMSM under the control of FCS-MPCC exhibits large overshoot at the transient and reached the current limit of the system, which further causes the control failure. It can be concluded from the presented results that a long prediction horizon benefits the FCS-MPCC in terms of the current ripple, since smaller TDD can be observed with similar switching frequencies. In Fig. 15, RFCS-MPCC produces smaller TDD at all working points than FCS-MPCC with the same switching frequencies or even FCS-MPCC with faster switching frequencies. Analogously, RFCS-MPCC reduces the TDD of the FCS-MPCC under the existence of the $L_{\mathrm{s}}$ mismatch at most working points. In summary, the proposed RFCS-MPCC yields smaller TDD than the FCS-MPCC for the most cases.

Finally, Table II compares the steady-state performance of conventional FCS-MPCC and the proposed RFCS-MPCC in terms of current TDD. For a fair comparison, TDDs with the same switching frequency and under $r_p = 100\%$ are considered. As can be seen, even when no mismatch exists, the proposed scheme, and thanks to the implemented optimal observer, can effectively tackle real-world nonidealities, unmodeled dynamics, etc., thus ensuring superior steady-state performance.

TABLE II
COMPARISON OF FCS-MPCC AND RFCS-MPCC FOR OPERATION AT THE SAME SWITCHING FREQUENCY AND $r_p = 100\%$

| Load | $N_p = 1$ | | $N_p = 5$ | |
|---|---|---|---|---|
| | RFCS-MPCC | FCS-MPCC | RFCS-MPCC | FCS-MPCC |
| 0 % | 19.64 | 28.07 | 14.50 | 15.35 |
| 50 % | 20.64 | 29.47 | 15.57 | 16.66 |
| 100 % | 23.22 | 36.52 | 17.66 | 19.06 |

### *E. Performance Under a Load Step*

In order to show the transient performance, RFCS-MPC and the conventional FCS-MPCC are tested under a load step from the no-load condition to the full-load condition, which is given at $t = 0.5$ s and a load step back to the no-load condition at $t = 1$ s.

A steady-state error can be observed in Fig. 17 at the no-load condition, which increases after the rated load torque is applied, i.e., between $t = 0.5$ s and $t = 1$ s. It can be explained by the fact that the model parameters used in the controller are potentially different from the real-motor parameters and vary with the operating points. In comparison to FCS-MPCC, the proposed RFCS-MPCC, as shown in Fig. 18, delivers more

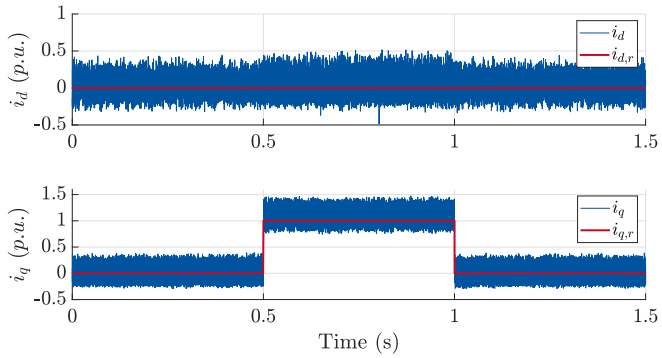


Fig. 17. Performance of FCS-MPCC with $N_p = 5$ under the load step.

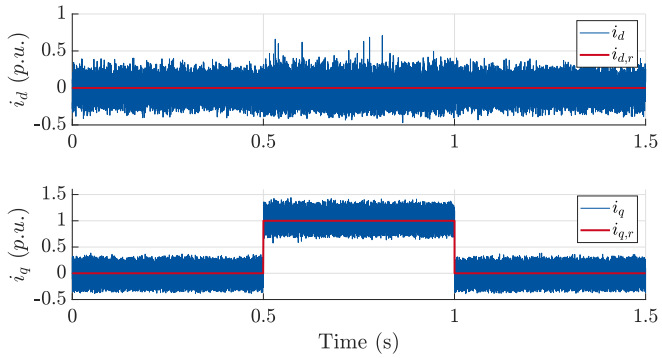


Fig. 18. Performance of the proposed RFCS-MPCC with $N_p = 5$ under the load step.

accurate tracking performance. It is noteworthy, however, that both controllers converge to the new reference value within 1 ms.

### F. Performance Under a Speed Ramp

The performance of the proposed RFCS-MPCC and FCS-MPCC is further tested under various speeds. A speed ramp from 300 to 2400 r/min is added at $t = 0.5$ s and lasts 0.12 s. The corresponding results are shown in Figs. 19 and 20, respectively.

It can be observed from the experimental results that RFCS-MPCC has improved the tracking accuracy over the whole range of examined speeds, for both $i_d$ and $i_q$. Moreover, the proposed RFCS-MPCC demonstrates more robust behavior during the acceleration.

### G. Computational Burden

Finally, the computational burden of the proposed dual reference frame RFCS-MPCC is investigated. It is quantified and represented by the turn around time. The corresponding measurements are shown in Fig. 21, where the RFCS-MPCC in the $dq$ reference frame and the proposed $\alpha\beta$ formulation are compared. The average, maximal, and minimal turnaround times are deployed to demonstrate the computational burden. Their development to the prediction horizon is also presented.

The proposed method allocates a great portion of matrix computation offline, which results in a significant reduction of the online computational burden of RFCS-MPCC. As shown in Fig. 21, the proposed solution can reduce the average turnaround

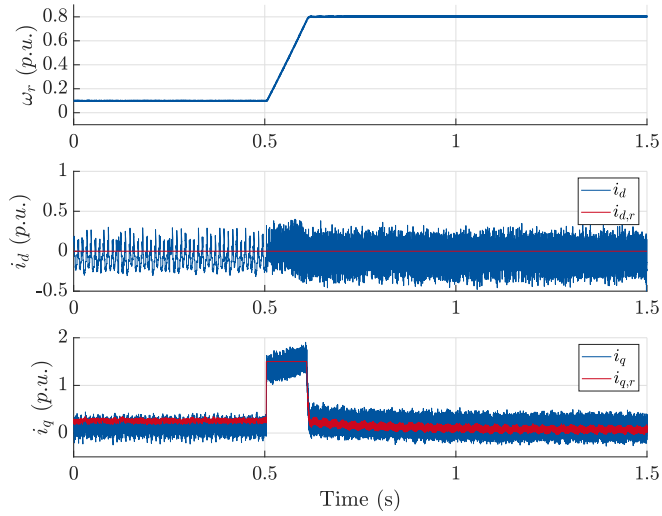


Fig. 19. Performance of the FCS-MPCC with $N_p = 5$ under the speed ramp. (a) Motor speed. (b) $d$-Current. (c) $q$-Current.

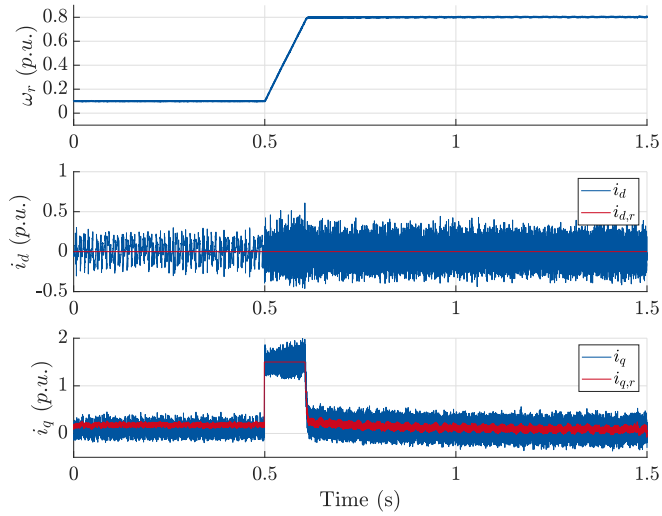


Fig. 20. Performance of the proposed RFCS-MPCC with $N_p = 5$ under the speed ramp.

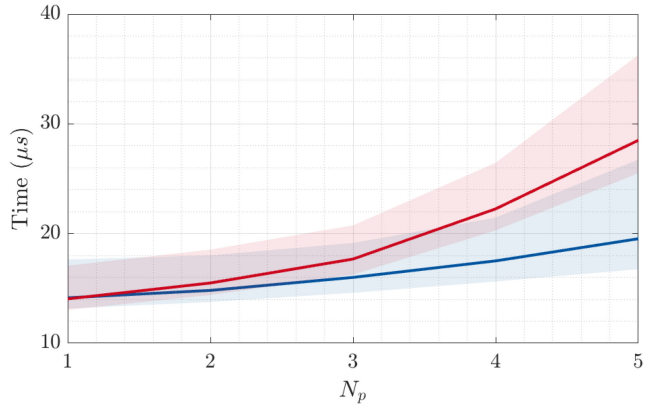


Fig. 21. Turn around time of the RFCS-MPCC problem formulated in the $\alpha\beta$ reference frame and the $dq$ reference frame. The proposed RFCS-MPCC problem formulation in the $\alpha\beta$ reference frame is presented in blue, where the averaged turnaround time is shown in solid line and the blue region is defined by the minimal and maximal turnaround time. The RFCS-MPCC problem in $dq$ reference frame is demonstrated in red.

time by almost 50%—as compared with a formulation exclusively in the $dq$-reference frame—for a prediction horizon of five steps. Moreover, for the same horizon length, the worst-case turn around time can be reduced by almost 30%, thus greatly facilitating the real-time implementation of the proposed RFCS-MPCC.

## VI. Conclusion

A robust long-horizon model predictive direct current control strategy for the SPMSM drive system is proposed. The disturbance, including the parameter mismatch and the unmodeled uncertainty, is treated as a constant within several sampling periods and estimated with the MHE. The impact of the parameter variations is investigated at different operating points. An obvious improvement of the proposed method can be observed at different parameter mismatch cases. The proposed method retains the stability of the control loop and alleviates the steady-state error caused by the parameter mismatch. Besides, the long-horizon direct current control problem is formulated in the $\alpha\beta$ domain, which therefore allocates some heavy computations to the offline preprocessing and reduces the online computational cost of solving the optimization problem. The computational burden is evaluated via the turnaround time in the dSPACE system. More specifically, the proposed control strategy can reduce the average turnaround time by almost 50% and the worst-case turn around time by almost 30% for a horizon of $N_p = 5$. The effectiveness of the proposed method is validated under various scenarios. Moreover, the feasibility of applying the proposed method for real-time implementation is verified with a sampling time of $50\,\mu$s for a prediction horizon of five.

## Appendix A

The matrices in (13) for MHE are given in the following:

$$\boldsymbol{\Pi}^F = \begin{bmatrix} \boldsymbol{C}\boldsymbol{A}^F \\ \boldsymbol{C}(\boldsymbol{A}^F)^2 \\ \vdots \\ \boldsymbol{C}(\boldsymbol{A}^F)^{N_e} \end{bmatrix}$$

$$\boldsymbol{\Lambda}^F = \begin{bmatrix} \boldsymbol{C}\boldsymbol{B}^F & \boldsymbol{0} & \dots & \boldsymbol{0} \\ \boldsymbol{C}\boldsymbol{A}^F\boldsymbol{B}^F & \boldsymbol{C}\boldsymbol{B}^F & \dots & \boldsymbol{0} \\ \vdots & \vdots & \ddots & \vdots \\ \boldsymbol{C}(\boldsymbol{A}^F)^{N_e-1}\boldsymbol{B}^F & \boldsymbol{C}(\boldsymbol{A}^F)^{N_e-2}\boldsymbol{B}^F & \dots & \boldsymbol{C}\boldsymbol{B}^F \end{bmatrix}$$

$$\boldsymbol{\Sigma}^F = \begin{bmatrix} \boldsymbol{C}\boldsymbol{I} \\ \boldsymbol{C}\boldsymbol{A}^F + \boldsymbol{C}\boldsymbol{I} \\ \vdots \\ \boldsymbol{C}(\boldsymbol{A}^F)^{N_e-1} + \boldsymbol{C}(\boldsymbol{A}^F)^{N_e-2} + \ldots + \boldsymbol{C}\boldsymbol{I} \end{bmatrix}$$

$$\boldsymbol{\Phi}^F = \begin{bmatrix} \boldsymbol{C}\boldsymbol{I} & \boldsymbol{0} & \dots & \boldsymbol{0} \\ \boldsymbol{C}\boldsymbol{A}^F & \boldsymbol{C}\boldsymbol{I} & \dots & \boldsymbol{0} \\ \vdots & \vdots & \ddots & \vdots \\ \boldsymbol{C}(\boldsymbol{A}^F)^{N_e-1} & \dots & \dots & \boldsymbol{C}\boldsymbol{I} \end{bmatrix}.$$

The matrices for RFCS-MPCC are shown as follows:

$$\boldsymbol{\Pi}^S = \begin{bmatrix} \boldsymbol{C}\boldsymbol{A}^S \\ \boldsymbol{C}(\boldsymbol{A}^S)^2 \\ \vdots \\ \boldsymbol{C}(\boldsymbol{A}^S)^{N_p} \end{bmatrix}, \boldsymbol{S} = \begin{bmatrix} \boldsymbol{I} & \boldsymbol{0} & \dots & \boldsymbol{0} \\ -\boldsymbol{I} & \boldsymbol{I} & \dots & \boldsymbol{0} \\ \boldsymbol{0} & -\boldsymbol{I} & \dots & \boldsymbol{0} \\ \vdots & \vdots & \ddots & \vdots \\ \boldsymbol{0} & \boldsymbol{0} & \dots & \boldsymbol{I} \end{bmatrix}, \boldsymbol{\delta} = \begin{bmatrix} \boldsymbol{I} \\ \boldsymbol{0} \\ \boldsymbol{0} \\ \vdots \\ \boldsymbol{0} \end{bmatrix}$$

$$\boldsymbol{\Upsilon} = \begin{bmatrix} \boldsymbol{C}\boldsymbol{B}^S\boldsymbol{T}_c & \boldsymbol{0} & \dots & \boldsymbol{0} \\ \boldsymbol{C}\boldsymbol{A}^S\boldsymbol{B}^S\boldsymbol{T}_c & \boldsymbol{C}\boldsymbol{B}^S\boldsymbol{T}_c & \dots & \boldsymbol{0} \\ \vdots & \vdots & \ddots & \vdots \\ \boldsymbol{C}(\boldsymbol{A}^S)^{N_p-1}\boldsymbol{B}^S\boldsymbol{T}_c & \dots & \dots & \boldsymbol{C}\boldsymbol{B}^S\boldsymbol{T}_c \end{bmatrix}$$

$$\boldsymbol{\Phi}^S = \begin{bmatrix} \boldsymbol{C}\boldsymbol{I} & \boldsymbol{0} & \dots & \boldsymbol{0} \\ \boldsymbol{C}\boldsymbol{A}^S & \boldsymbol{C}\boldsymbol{I} & \dots & \boldsymbol{0} \\ \vdots & \vdots & \ddots & \vdots \\ \boldsymbol{C}(\boldsymbol{A}^S)^{N_p-1} & \dots & \dots & \boldsymbol{C}\boldsymbol{I} \end{bmatrix},$$

$$\boldsymbol{T} = \begin{bmatrix} \boldsymbol{T}_{p,k}^{-1} \\ \boldsymbol{T}_{p,k+1}^{-1} \\ \vdots \\ \boldsymbol{T}_{p,k+N_p-1}^{-1} \end{bmatrix}.$$

## References


[1] P. Cortes, M. P. Kazmierkowski, R. M. Kennel, D. E. Quevedo, and J. Rodriguez, "Predictive control in power electronics and drives," *IEEE Trans. Ind. Electron.*, vol. 55, no. 12, pp. 4312–4324, Dec. 2008.

[2] V. Yaramasu, M. Rivera, B. Wu, and J. Rodriguez, "Model predictive current control of two-level four-leg inverters—Part I: Concept, algorithm, and simulation analysis," *IEEE Trans. Power Electron.*, vol. 28, no. 7, pp. 3459–3468, Jul. 2013.

[3] W. Xie, X. Wang, F. Wang, W. Xu, R. Kennel, and D. Gerling, "Dynamic loss minimization of finite control set-model predictive torque control for electric drive system," *IEEE Trans. Power Electron.*, vol. 31, no. 1, pp. 849–860, Jan. 2016.

[4] F. Morel, X. Lin-Shi, J. Retif, B. Allard, and C. Buttay, "A comparative study of predictive current control schemes for a permanent-magnet synchronous machine drive," *IEEE Trans. Ind. Electron.*, vol. 56, no. 7, pp. 2715–2728, Jul. 2009.

[5] M. Preindl and S. Bolognani, "Comparison of direct and PWM model predictive control for power electronic and drive systems," in *Proc. 28th Annu. IEEE Appl. Power Electron. Conf. Expo.*, 2013, pp. 2526–2533.

[6] A. A. Ahmed, B. K. Koh, and Y. I. Lee, "A comparison of finite control set and continuous control set model predictive control schemes for speed control of induction motors," *IEEE Trans. Ind. Informat.*, vol. 14, no. 4, pp. 1334–1346, Apr. 2018.

[7] R. Vargas, P. Cortes, U. Ammann, J. Rodriguez, and J. Pontt, "Predictive control of a three-phase neutral-point-clamped inverter," *IEEE Trans. Ind. Electron.*, vol. 54, no. 5, pp. 2697–2705, Oct. 2007.

[8] V. Yaramasu and B. Wu, "Predictive control of a three-level boost converter and an NPC inverter for high-power PMSG-based medium voltage wind energy conversion systems," *IEEE Trans. Power Electron.*, vol. 29, no. 10, pp. 5308–5322, Oct. 2014.
[9] M. Narimani, B. Wu, V. Yaramasu, Z. Cheng, and N. R. Zargari, "Finite control-set model predictive control (FCS-MPC) of nested neutral point-clamped (NNPC) converter," *IEEE Trans. Power Electron.*, vol. 30, no. 12, pp. 7262–7269, Dec. 2015.
[10] Z. Zhang, C. M. Hackl, and R. Kennel, "Computationally efficient DMPC for three-level NPC back-to-back converters in wind turbine systems with PMSG," *IEEE Trans. Power Electron.*, vol. 32, no. 10, pp. 8018–8034, Oct. 2017.
[11] M. Siami, D. Arab Khaburi, and J. Rodriguez, "Simplified finite control set-model predictive control for matrix converter-fed PMSM drives," *IEEE Trans. Power Electron.*, vol. 33, no. 3, pp. 2438–2446, Mar. 2018.
[12] P. Karamanakos and T. Geyer, "Guidelines for the design of finite control set model predictive controllers," *IEEE Trans. Power Electron.*, vol. 35, no. 7, pp. 7434–7450, Jul. 2020.
[13] T. Geyer, P. Karamanakos, and R. Kennel, "On the benefit of long-horizon direct model predictive control for drives with LC filters," in *Proc. IEEE Energy Convers. Congr. Expo.*, 2014, pp. 3520–3527.
[14] C. Bordons and C. Montero, "Basic principles of MPC for power converters: Bridging the gap between theory and practice," *IEEE Ind. Electron. Mag.*, vol. 9, no. 3, pp. 31–43, Sep. 2015.
[15] T. Geyer and D. E. Quevedo, "Multistep finite control set model predictive control for power electronics," *IEEE Trans. Power Electron.*, vol. 29, no. 12, pp. 6836–6846, Dec. 2014.
[16] P. Karamanakos, T. Geyer, and S. Manias, "Direct voltage control of dc–dc boost converters using enumeration-based model predictive control," *IEEE Trans. Power Electron.*, vol. 29, no. 2, pp. 968–978, Feb. 2014.
[17] T. Geyer, "Computationally efficient model predictive direct torque control," *IEEE Trans. Power Electron.*, vol. 26, no. 10, pp. 2804–2816, Oct. 2011.
[18] H. A. Young, M. A. Perez, and J. Rodriguez, "Analysis of finite-control-set model predictive current control with model parameter mismatch in a three-phase inverter," *IEEE Trans. Ind. Electron.*, vol. 63, no. 5, pp. 3100–3107, May 2016.
[19] L. Ortombina, P. Karamanakos, and M. Zigliotto, "Robustness analysis of long-horizon direct model predictive control: Permanent magnet synchronous motor drives," in *Proc. IEEE 21st Workshop Control Model. Power Electron.*, 2020, pp. 1–8.
[20] C. Lin, J. Yu, Y. Lai, and H. Yu, "Improved model-free predictive current control for synchronous reluctance motor drives," *IEEE Trans. Ind. Electron.*, vol. 63, no. 6, pp. 3942–3953, Jun. 2016.
[21] X. Yuan, S. Zhang, and C. Zhang, "Nonparametric predictive current control for PMSM," *IEEE Trans. Power Electron.*, vol. 35, no. 9, pp. 9332–9341, Sep. 2020.
[22] M. Siami, D. A. Khaburi, and J. Rodríguez, "Torque ripple reduction of predictive torque control for PMSM drives with parameter mismatch," *IEEE Trans. Power Electron.*, vol. 32, no. 9, pp. 7160–7168, Sep. 2017.
[23] M. Preindl, "Robust control invariant sets and Lyapunov-based MPC for IPM synchronous motor drives," *IEEE Trans. Ind. Electron.*, vol. 63, no. 6, pp. 3925–3933, Jun. 2016.
[24] X. Liu, L. Zhou, J. Wang, X. Gao, Z. Li, and Z. Zhang, "Robust predictive current control of permanent-magnet synchronous motors with newly designed cost function," *IEEE Trans. Power Electron.*, vol. 35, no. 10, pp. 10778–10788, Oct. 2020.
[25] X. Zhang, L. Zhang, and Y. Zhang, "Model predictive current control for PMSM drives with parameter robustness improvement," *IEEE Trans. Power Electron.*, vol. 34, no. 2, pp. 1645–1657, Feb. 2019.
[26] S. Liu and C. Liu, "Virtual-vector-based robust predictive current control for dual three-phase PMSM," *IEEE Trans. Ind. Electron.*, vol. 68, no. 3, pp. 2048–2058, Mar. 2021.
[27] F. Wang, J. Wang, R. M. Kennel, and J. Rodríguez, "Fast speed control of ac machines without the proportional-integral controller: Using an extended high-gain state observer," *IEEE Trans. Power Electron.*, vol. 34, no. 9, pp. 9006–9015, Sep. 2019.
[28] O. Wallscheid and E. F. B. Ngoumtsa, "Investigation of disturbance observers for model predictive current control in electric drives," *IEEE Trans. Power Electron.*, vol. 35, no. 12, pp. 13563–13572, Dec. 2020.
[29] D. Schröder, *Elektrische Antriebe - Regelung Von Antriebssystemen*. Berlin, Germany: Springer, 2009.
[30] A. Andersson and T. Thiringer, "Assessment of an improved finite control set model predictive current controller for automotive propulsion applications," *IEEE Trans. Ind. Electron.*, vol. 67, no. 1, pp. 91–100, Jan. 2020.
[31] F. Toso, D. Da Ru, P. Alotto, and S. Bolognani, "A moving horizon estimator for the speed and rotor position of a sensorless PMSM drive," *IEEE Trans. Power Electron.*, vol. 34, no. 1, pp. 580–587, Jan. 2019.
[32] D. Frick, A. Domahidi, M. Vukov, S. Mariethoz, M. Diehl, and M. Morari, "Moving horizon estimation for induction motors," in *Proc. 3rd IEEE Int. Symp. Sensorless Control Elect. Drives*, 2012, pp. 1–6.
[33] P. Kühl, M. Diehl, T. Kraus, J. P. Schlöder, and H. G. Bock, "A real-time algorithm for moving horizon state and parameter estimation," *Comput. Chem. Eng.*, vol. 35, no. 1, pp. 71–83, 2011. [Online]. Available: http://www.sciencedirect.com/science/article/pii/S0098135410002607
[34] C. V. Rao, J. B. Rawlings, and D. Q. Mayne, "Constrained state estimation for nonlinear discrete-time systems: Stability and moving horizon approximations," *IEEE Trans. Autom. Control*, vol. 48, no. 2, pp. 246–258, Feb. 2003.
[35] X. Li, W. Tian, X. Gao, Q. Yang, and R. Kennel, "A generalized observer-based robust predictive current control strategy for PMSM drive system," *IEEE Trans. Ind. Electron.*, pp. 1–1, 2021, doi: 10.1109/TIE.2021.3062271.

**Xinyue Li** (Graduate Student Member, IEEE) was born in Yunnan, China, in 1991. She received the B.S. degree in electrical engineering from Tsinghua University, Beijing, China, in 2013, and the M.S. degree in electrical engineering, information technology, and computer engineering from RWTH Aachen University, Aachen, Germany, in 2017. She is currently working toward the Dr.Ing. (Ph.D.) degree with the Institute for Electrical Drive Systems and Power Electronics, Technical University of Munich, Munich, Germany.

Since 2017, she has been with Research and Development Department, Bosch Rexroth AG, Lohr am Main, Germany. Her research interests include parameter identification, robust, and optimal control of ac machines.

**Qifan Yang** (Graduate Student Member, IEEE) was born in Anqing, Anhui, China, in 1995. He received the B.Eng. degree in electrical engineering, in 2016, from Xi'an Jiaotong University, Xi'an, China, and the M.Sc. degree in electrical power engineering, in 2019, from the Technical University of Munich, Munich, Germany, where he is currently working toward the Ph.D. degree with the Chair of Electrical Drive Systems and Power Electronics.

His research interests include optimal control, power electronics, and electrical drives.

**Wei Tian** (Graduate Student Member, IEEE) was born in Taizhou, Jiangsu, China, in 1989. He received the B.Eng. degree in electrical engineering and automation from Central South University (CSU), Changsha, China, in 2012, and the M.Sc. degree in electrical power engineering from RWTH Aachen University, Aachen, Germany, in 2015. He is currently working toward the Ph.D. degree with the Chair of Electrical Drive Systems and Power Electronics, Technical University of Munich (TUM), Munich, Germany.

His research interests include power electronics and electrical drives, model predictive control, and modular multilevel converter.

**Petros Karamanakos** (Senior Member, IEEE) received the Diploma and Ph.D. degrees in electrical and computer engineering from the National Technical University of Athens (NTUA), Athens, Greece, in 2007 and 2013, respectively.

From 2010 to 2011, he was with ABB Corporate Research Center, Baden-Dättwil, Switzerland, where he worked on model predictive control strategies for medium-voltage drives. From 2013 to 2016, he was a PostDoc Research Associate with the Chair of Electrical Drive Systems and Power Electronics, Technische Universität München, Munich, Germany. Since September 2016, he has been an Assistant Professor with the Faculty of Information Technology and Communication Sciences, Tampere University, Tampere, Finland. His research interests include the intersection of optimal control, mathematical programming, and power electronics, including model predictive control and optimal modulation for power electronic converters and ac variable speed drives.

Dr. Karamanakos was a recipient of the 2014 Third Best Paper Award of the IEEE TRANSACTIONS ON INDUSTRY APPLICATIONS and two Prize Paper Awards at conferences. He is an Associate Editor of the IEEE TRANSACTIONS ON INDUSTRY APPLICATIONS and the *IEEE Open Journal of Industry Applications*.

**Ralph Kennel** (Senior Member, IEEE) was born in Kaiserslautern, Germany, in 1955. He received the diploma and the Dr.-Ing. (Ph.D.) degrees from the University of Kaiserslautern, Kaiserslautern, Germany, in 1979 and 1984, respectively.

From 1983 to 1999, he was with Robert BOSCH GmbH, Germany, working on several positions. Until 1997, he was responsible for the development of servo drives. From 1994 to 1999, he was a Visiting Professor with the University of Newcastle-upon-Tyne, Newcastle-upon-Tyne, U.K. From 1999 to 2008, he was a Professor of electrical machines and drives with Wuppertal University, Wuppertal, Germany. Since 2008, he has been a Professor of electrical drive systems and power electronics with the Technical University of Munich, Munich, Germany. His research interests include sensorless control of ac drives, predictive control of power electronics, and hardware-in-the-loop systems.

Dr. Kennel is a Fellow of IET (former IEE) and a Chartered Engineer in the U.K.. Within IEEE, he was Treasurer of the Germany Section as well as ECCE Global Partnership Chair of the Power Electronics society. He is an Associate Editor for the IEEE TRANSACTIONS ON POWER ELECTRONICS.